
Consistent World Models via Foresight Diffusion

Yu Zhang*, Xingzhuo Guo*, Haoran Xu, Mingsheng Long[✉]

School of Software, BNRist, Tsinghua University, China

{zhangyu24, gxz23, xu-hr22}@mails.tsinghua.edu.cn, mingsheng@tsinghua.edu.cn

Abstract

Diffusion and flow-based models have enabled significant progress in generation tasks across various modalities and have recently found applications in world modeling. However, unlike typical generation tasks that encourage sample diversity, world models entail different sources of uncertainty and require consistent samples aligned with the ground-truth trajectory, which is a limitation we empirically observe in diffusion models. We argue that a key bottleneck in learning consistent diffusion-based world models lies in the suboptimal predictive ability, which we attribute to the entanglement of condition understanding and target denoising within shared architectures and co-training schemes. To address this, we propose *Foresight Diffusion (ForeDiff)*, a diffusion-based world modeling framework that enhances consistency by decoupling condition understanding from target denoising. ForeDiff incorporates a separate deterministic predictive stream to process conditioning inputs independently of the denoising stream, and further leverages a pretrained predictor to extract informative representations that guide generation. Extensive experiments on robot video prediction and scientific spatiotemporal forecasting show that ForeDiff improves both predictive accuracy and sample consistency over strong baselines, offering a promising direction for diffusion-based world models.

1 Introduction

Diffusion models [33, 34, 16, 35] and flow-based models [22, 23, 3] are a class of generative models that produce high-fidelity samples by progressively denoising corrupted data. This modeling paradigm has achieved state-of-the-art across a wide range of tasks and modalities, including image [10], video [17], and cross-modal generation [30, 32, 28]. Owing to their ability to model complex and multimodal distributions, diffusion models have recently been adopted for world modeling [38, 8, 13] within the conditional generation framework, where they serve as spatiotemporal predictors that learn real-world physical dynamics and generate future trajectories conditioned on past observations.

Though both tasks demand high-fidelity outputs, world modeling fundamentally differs from conventional generative tasks where diffusion and flow-based models have excelled. Generative tasks (e.g., text-to-image synthesis) operate under inherently stochastic target distributions, where prompts or class labels correspond to a broad spectrum of plausible outputs. In contrast, world models (e.g., robot video prediction) aim to infer physically coherent futures from past observations, where uncertainty primarily stems from incomplete or partial information. Consequently, the generated samples are expected to closely align with ground-truth trajectories, rather than exhibit diverse modes.

These fundamental differences also lead to distinct evaluation criteria. Generative tasks emphasize diversity and perceptual quality, often tolerating imperfection in individual samples. In contrast, world models prioritize accuracy and consistency, where *consistency* refers to the model’s ability to produce low-variance outputs under identical conditions, ensuring that each sample remains plausible and physically grounded. In such settings, every sample matters.

*Equal contribution.

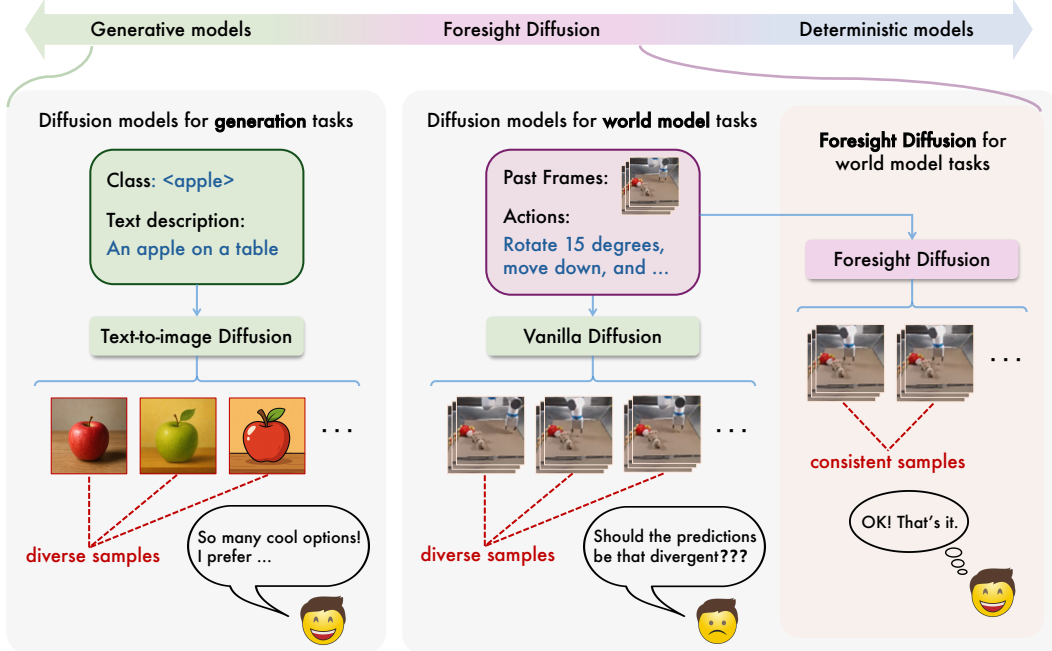


Figure 1: Aligning model stochasticity with task demands. (Left) Generation tasks favor diversity, making diffusion models ideal for producing varied samples. (Middle) In contrast, world model tasks require a balance between generation and prediction, and vanilla diffusion models demonstrate unsatisfactory sample consistency. (Right) Foresight Diffusion achieves a midpoint between highly stochastic generative models and fully deterministic models, making it well-suited for world modeling.

This notion of consistency is especially critical in world modeling tasks, where downstream planning or control may rely on stable predictive behavior across samples [15, 12], and it imposes specific demands on the capabilities of world models when employing diffusion models, which are prone to issues such as hallucinations, weak conditioning, and sample instability [2, 10]. As illustrated in Figure 2, although vanilla diffusion models outperform traditional autoregressive models in terms of best-case as well as average performance, they exhibit higher sample variance and heavier worst-case tails that are undesirable for world modeling. This highlights a fundamental mismatch between vanilla diffusion models and the requirements of world modeling tasks, and consequently there remains a need for sample-consistent diffusion models that effectively balance stochasticity and determinism.

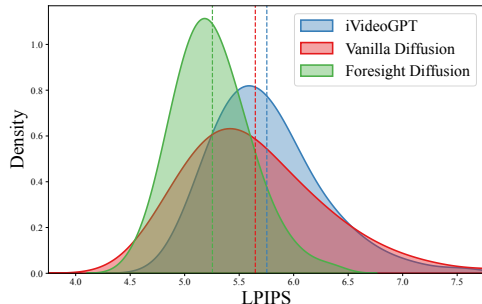


Figure 2: Kernel density estimation curves of sample-wise LPIPS distributions. Shaded areas represent estimated probability densities; dashed lines indicate sample means. Lower LPIPS scores correspond to better quality.

To address these challenges, we propose *Foresight Diffusion (ForeDiff)*, a framework designed to enhance the consistency of diffusion-based world models by decoupling condition understanding from the denoising process. Diffusion models typically exhibit suboptimal predictive ability compared to deterministic approaches, as condition understanding and target denoising are entangled within shared architectures and co-training schemes, which impairs effective condition understanding. Instead of directly applying a conventional conditional diffusion model, ForeDiff introduces a separate deterministic stream that processes condition inputs independently of the stochastic denoising stream. Furthermore, it leverages a pretrained deterministic predictor to extract informative representations, thereby improving the model’s predictive ability. Experiments across multiple modalities demonstrate that ForeDiff significantly improves both predictive performance and sample consistency.

Our contributions are summarized as follows:

- We revisit diffusion models in the context of world modeling, a task different from conventional generation, and identify that vanilla diffusion models exhibit consistency issues.
- We attribute the consistency issues of diffusion models to the entanglement of condition understanding and target denoising within shared architectures and co-training schemes.
- We propose Foresight Diffusion (ForeDiff), a framework that improves consistency by decoupling condition understanding and incorporating a pretrained deterministic predictor.
- Extensive experiments and analyses on video prediction and spatiotemporal forecasting demonstrate that ForeDiff achieves superior predictive accuracy and sample consistency.

2 Preliminaries

Denoising-based generative models [16, 35, 19, 4] have gained significant attention for modeling complex data distributions. These models typically rely on a forward trajectory that progressively corrupts clean data samples with increasing amounts of noise. The forward process can be expressed as a interpolation between a clean sample $\mathbf{x}_0 \sim q(\mathbf{x})$ and standard Gaussian noise $\epsilon \sim \mathcal{N}(\mathbf{0}, \mathbf{I})$:

$$\mathbf{x}_t = \alpha_t \mathbf{x}_0 + \sigma_t \epsilon, \quad t \in [0, 1]. \quad (1)$$

In this work, we adopt a simple linear interpolation scheme known as rectified flow [22, 23], which has been widely used due to its analytical tractability and connections to optimal transport. The rectified forward process is defined as

$$\mathbf{x}_t = (1 - t)\mathbf{x}_0 + t\epsilon. \quad (2)$$

To recover the data distribution, we learn to reverse this process by training a neural network $\mathbf{v}_\theta(\mathbf{x}_t, t)$ to approximate the time-dependent velocity field (or one of its reparameterizations). The training objective, known as conditional flow matching, is formulated as:

$$\mathcal{L}_{\text{velocity}}(\theta) := \mathbb{E}_{\mathbf{x}_0, \epsilon, t} \left[\|\mathbf{v}_\theta(\mathbf{x}_t, t) - (-\mathbf{x}_0 + \epsilon)\|^2 \right]. \quad (3)$$

At inference time, samples are generated by integrating the learned velocity field backward in time:

$$\mathbf{x}_{t-\Delta t} = \mathbf{x}_t - \mathbf{v}_\theta(\mathbf{x}_t, t)\Delta t, \quad (4)$$

starting from a Gaussian noise sample $\mathbf{x}_1 \sim \mathcal{N}(\mathbf{0}, \mathbf{I})$ and progressing toward $t = 0$. This framework naturally extends to conditional generation by introducing conditioning variables \mathbf{c} into the model, resulting in a conditional velocity field $\mathbf{v}_\theta(\mathbf{x}_t, t, \mathbf{c})$, where \mathbf{c} guides the generative dynamics.

3 Method

3.1 Diffusion Models for World Model Tasks

World modeling is fundamentally a prediction task with stochasticity. We formulate it as a conditional generation problem, where $\mathbf{s}^{-O+1:0}$ denotes a sequence of past visual observations and \mathbf{c} represents a potential perturbation to the environment (e.g., actions or goals) [1]. The objective of a world model is to approximate the conditional distribution of future frames $p(\mathbf{s}^{1:S} \mid \mathbf{s}^{-O+1:0}, \mathbf{c})$, which is inherently unknown and must be learned from data.

To reduce computational cost, we adopt the widely used latent diffusion paradigm [29], which compresses the frames into a lower-dimensional latent space using a pretrained autoencoder composed of an encoder E and a decoder D . The past and future frames are encoded as $\mathbf{z}^{-O+1:0} = E(\mathbf{s}^{-O+1:0})$ and $\mathbf{z}^{1:S} = E(\mathbf{s}^{1:S})$, respectively. Denoting $\mathbf{x} = \mathbf{z}^{1:S}$ and $\mathbf{y} = \{\mathbf{z}^{-O+1:0}, \mathbf{c}\}$, the learning objective becomes modeling the conditional distribution $p(\mathbf{x} \mid \mathbf{y})$. We focus on diffusion-based world models, which—as described in Section 2—learn a conditional denoiser $\mathbf{v}_\theta(\mathbf{x}_t, \mathbf{y}, t)$ that takes as input both the condition \mathbf{y} and a noisy version of the target \mathbf{x}_t .

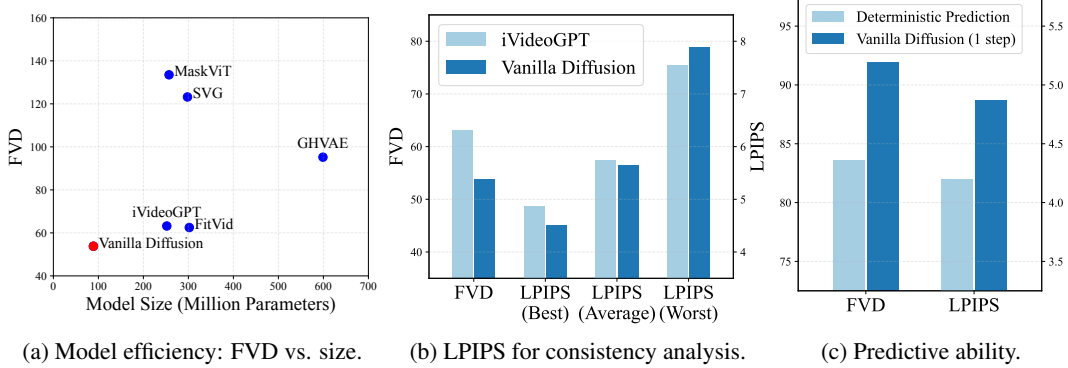


Figure 3: Comparison between diffusion-based world models and existing baselines. (a) Vanilla diffusion achieves competitive FVD with significantly fewer parameters, demonstrating high model efficiency. (b) Vanilla diffusion performs well on best and average LPIPS, but suffers from higher worst-case error, highlighting poor sample consistency. (c) Vanilla diffusion underperforms a deterministic predictor in absence of noisy targets, revealing its limited predictive ability.

Diffusion world models are efficient, accurate, but not consistent. We evaluate the performance of diffusion-based world models in comparison to existing baselines, including auto-regressive and mask-based architectures [42, 14]. We adopt a video-adapted DiT, shown in Figure 4(a), as our vanilla diffusion model, and assess its performance using two standard metrics: Fréchet Video Distance (FVD) for distributional similarity, and LPIPS for perceptual sample-level quality [36, 46]. Figure 3a presents a scatter plot comparing model size and FVD, while LPIPS scores under best-case, average, and worst-case conditions are reported in Figure 3b. Our key findings are summarized below:

- Despite having a smaller model size and no pretraining, the vanilla diffusion model outperforms baseline models in FVD, best-case LPIPS, and average LPIPS, demonstrating strong efficiency and accuracy for world modeling.
- However, under worst-case LPIPS, the diffusion model underperforms iVideoGPT. Together with the results in Figure 2, this suggests a lack of sample consistency, i.e., insufficient concentration of plausible outputs under the same condition.

These results reveal a critical limitation of diffusion-based world models: although they exhibit strong best-case performance with compact architectures, they lack robust conditional control during generation, leading to significant variability across samples. As a result, evaluating only best-case performance—as commonly done in prior works [38, 45, 42]—can be misleading. Unless otherwise specified, we report average metrics throughout the remainder of the paper.

3.2 Observations

To further explore the sample inconsistency behavior in diffusion-based world models, we investigate their predictive ability, i.e., how well the model understands condition inputs (e.g., visual observations and actions) and predicts future trajectories based on the task’s underlying dynamics. To assess how much the model relies solely on \mathbf{y} during denoising, we consider the special case at $t = 1$ (corresponding to $t = T$ under notations in DDPM [16]), where $\mathbf{x}_1 \sim \mathcal{N}(\mathbf{0}, \mathbf{I})$ contains no signal and thus contributes no useful information, which introduces the following lemma²:

Lemma 3.1. *For a diffusion model as defined in Section 2, by reparameterizing the output as $\hat{\mathbf{x}}_\theta(\mathbf{x}_t, t, \mathbf{y}) = \mathbf{x}_t - t \cdot \mathbf{v}_\theta(\mathbf{x}_t, t, \mathbf{y})$ [19], the training objective at $t = 1$ simplifies to:*

$$\mathcal{L}_{\text{pred}}(\theta|t=1) = \mathbb{E}_{\mathbf{x}_0, \mathbf{y}, \epsilon} \left[\|\hat{\mathbf{x}}_\theta(\epsilon, 1, \mathbf{y}) - \mathbf{x}_0\|_2^2 \right], \quad (5)$$

where the noise ϵ is independent of both \mathbf{x}_0 and \mathbf{y} . Furthermore, a diffusion model minimizing Eq. (5) reduces to a similar architected deterministic predictor f_ξ minimizing the following objective:

$$\mathcal{L}_{\text{deter}}(\xi) = \mathbb{E}_{\mathbf{x}_0, \mathbf{y}} \left[\|f_\xi(\mathbf{y}) - \mathbf{x}_0\|_2^2 \right]. \quad (6)$$

²Proof is referred to Appendix A.

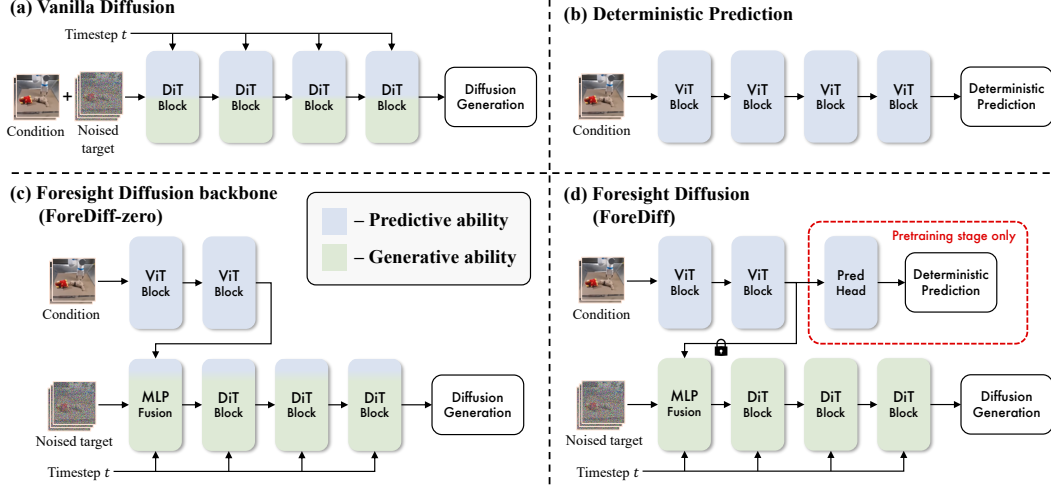


Figure 4: Overview of Foresight Diffusion. (a) Vanilla diffusion jointly processes condition and noisy target, limiting its predictive ability. (b) A Deterministic model focuses solely on condition understanding and achieves better predictive performance. (c) ForeDiff-zero introduces a separate predictive stream to isolate condition understanding from noise. (d) ForeDiff further adopts a two-stage scheme: it pre-trains the predictive stream, then freezes its representations to guide generation.

This lemma conveys two insights. First, evaluating performance at $t = 1$ provides a reasonable proxy for assessing the predictive ability of a diffusion model, as the model must rely entirely on \mathbf{y} while discarding the irrelevant input ϵ . Second, the predictive ability of a diffusion model is inherently bounded and is possible to be equivalent to that of a deterministic model. To empirically test whether the diffusion model can reach this upper bound, we train a ViT-based deterministic model f_ξ , shown in Figure 4(b), with an architecture analogous to the diffusion model. We then compare its performance to the diffusion model evaluated with a single-step inference. The results, shown in Figure 3c, reveal that the diffusion model underperforms significantly compared to its deterministic counterpart, highlighting its limited predictive ability relative to its potential.

Discussion. Such observation indicates that the suboptimal predictive ability of diffusion models stems from the entanglement between condition understanding and target denoising due to the nature of diffusion models to train on various t . This entanglement constrains condition understanding by factors of both architecture and training. From the architecture perspective, network parameters must simultaneously learn both condition understanding of \mathbf{y} and target denoising of \mathbf{x}_t , and this dual-role constraint can limit the model’s ability to fully exploit the condition information. From the training perspective, the presence of \mathbf{x}_t as an informative input introduces a shortcut, making it easier for the model to rely on generative priors from \mathbf{x}_t rather than precise task-specific dynamics from \mathbf{y} .

3.3 Foresight Diffusion

Previous observations suggest that shared architectures and co-training schemes of condition \mathbf{y} and noisy target \mathbf{x}_t limit the predictive ability of diffusion models, due to the need to simultaneously balance condition understanding and target denoising. To address these limitations, we introduce a simple yet effective framework that enhances predictive ability through architectural decoupling and improved training scheme.

Architecture. Building on architectures of vanilla diffusion models, we propose an architectural extension that integrates decoupled deterministic blocks for processing the condition \mathbf{y} independently of \mathbf{x}_t . This design forms the *Foresight Diffusion backbone (ForeDiff-zero)*, illustrated in Figure 4(c), which separates the model into two distinct streams, the predictive stream and the generative stream, aiming to focus on \mathbf{y} and \mathbf{x}_t respectively. The predictive stream is composed of deterministic ViT blocks, while the generative stream follows the standard DiT-based denoising process. Formally, let M denote the number of ViT blocks and N the number of DiT blocks. The process can then be

formulated as:

$$\begin{aligned} \mathbf{g}_0 &= \text{PatchEmbed}(\mathbf{y}), & \mathbf{g}_i &= \text{ViT}_i(\mathbf{g}_{i-1}), \quad i = 1, \dots, M, \\ \mathbf{h}_0 &= \text{PatchEmbed}(\mathbf{x}_t), & \mathbf{h}_1 &= \text{Fusion}(\mathbf{h}_0, \mathbf{g}_M, t), \\ \mathbf{h}_{i+1} &= \text{DiT}_i(\mathbf{h}_i, t), \quad i = 1, \dots, N, & \hat{\mathbf{v}} &= \text{OutHead}(\mathbf{h}_{N+1}). \end{aligned} \quad (7)$$

When $M = 0$, ForeDiff-zero reduces to vanilla conditional diffusion, where the fusion operates directly on the raw condition: $\mathbf{h}_1 = \text{Fusion}(\mathbf{h}_0, \text{PatchEmbed}(\mathbf{y}), t)$.

Unlike vanilla diffusion models, which ingest both \mathbf{y} and \mathbf{x}_t at the initial point of a shared network, ForeDiff-zero processes the condition solely within its predictive stream and passes the resulting informative representation \mathbf{g}_M instead of \mathbf{y} to the generative stream. Since the predictive stream is entirely agnostic to \mathbf{x}_t , its parameters are fully dedicated to understanding \mathbf{y} , thereby mitigating the architectural entanglement that limits the predictive ability.

Training scheme. To further ensure that the ViT blocks in the predictive stream effectively acquire predictive ability, in addition to the end-to-end training scheme of ForeDiff-zero, we further enhance *Foresight Diffusion (ForeDiff)* by adopting a two-stage training scheme demonstrated in Figure 4(d). In the first stage, the predictive stream is trained as a standalone deterministic predictor. Inspired by the strong predictive ability of the deterministic model f_ξ discussed in Section 3.2, ForeDiff trains the predictive stream by adding an additional module PredHead as an prediction head to form the architecture of f_ξ , which is defined by $f_\xi(\mathbf{y}) = \text{PredHead}(\mathbf{g}_M)$. The training objective follows the simplest prediction loss in Eq. (6). In the second stage, we freeze the pretrained predictive stream and remove the PredHead module. The resulting internal representation \mathbf{g}_M , computed by the frozen ViT blocks, is then used as the conditioning input to train the generative stream.

We treat the predictive and generative streams as two independent models, denoted by P_ξ and G_θ , respectively. Each stage is optimized with one of the following loss functions:

$$\begin{aligned} \mathcal{L}_{\text{deter}} &= \mathbb{E}_{\mathbf{x}_0, \mathbf{y}} \left[\|P_\xi(\mathbf{y}) - \mathbf{x}_0\|_2^2 \right], \\ \mathcal{L}_{\text{denoise}} &= \mathbb{E}_{\mathbf{x}_0, \mathbf{y}, \epsilon, t} \left[\|G_\theta(\mathbf{x}_t, P'_\xi(\mathbf{y}), t) - (-\mathbf{x}_0 + \epsilon)\|_2^2 \right], \end{aligned} \quad (8)$$

where P'_ξ refers to the predictive stream excluding the PredHead module. This ensures that the features guiding generation are derived from the learned predictive representations, rather than the final prediction outputs. By combining architectural decoupling with dedicated predictive pretraining, ForeDiff leverages a deterministic predictor as a preparatory module for conditional generation. The design enables the model to “foresee” contextually rich representations, thereby enhancing predictive ability and improving both generation accuracy and sample consistency.

4 Experiments

We evaluate Foresight Diffusion in comparison to conventional conditional diffusion baselines across a range of tasks, covering both (action-conditioned) robot video prediction and scientific spatiotemporal forecasting. We adopt the same model architecture across all tasks, with the only difference being the condition information provided to the model. The model components follow the standard configurations of ViT [11] and DiT [27] (or SiT [25]) blocks. Unless otherwise specified, we use 6 ViT blocks in the predictive stream and 12 DiT blocks in the generative stream. Additional implementation details are provided in Appendix B.

4.1 Robot Video Prediction

Setup. We begin by evaluating on RoboNet[9] and RT-1[7], two real-world video datasets widely used for assessing general video prediction performance. RoboNet contains 162k videos collected from 7 robots operating in diverse environments. Following previous works [5, 42], the task is to predict 10 future frames given 2 past frames together with actions. RT-1 consists of 87k videos from 13 robots performing hundreds of real-world tasks. Here, the objective is to predict 14 future frames conditioned on 2 past frames and the corresponding instructions. All video frames are resized to 64×64 pixels for both datasets. We evaluate model performance using widely adopted metrics including FVD [36], PSNR [18], SSIM [40], and LPIPS [46]. In addition, we introduce STD_{PSNR} ,

Table 1: Robot video prediction results on RoboNet and RT-1 datasets. SSIM and LPIPS scores are scaled by 100 for convenient display.

Dataset	Method	FVD ↓	PSNR ↑	SSIM ↑	LPIPS ↓	STD _{PSNR} ↓	STD _{SSIM} ↓	STD _{LPIPS} ↓
RoboNet	Vanilla Diffusion	53.8	27.1	88.2	5.65	0.66	1.33	0.65
	ForeDiff-zero	52.7	27.2	88.4	5.54	0.68	1.36	0.66
	ForeDiff	51.5	27.4	88.8	5.25	0.37	0.70	0.35
RT-1	Vanilla Diffusion	11.7	30.4	93.6	3.79	0.97	1.11	0.53
	ForeDiff-zero	11.1	30.7	93.9	3.60	0.95	1.03	0.50
	ForeDiff	12.0	31.2	94.4	3.42	0.38	0.33	0.17

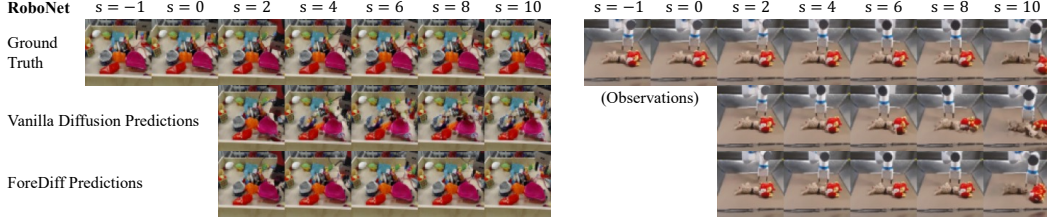


Figure 5: Visualization of results on RoboNet dataset (zoom in for details). In vanilla diffusion models, the pink shovel (left) appears distorted, while the toy object (right) collapses entirely. In contrast, ForeDiff produces more structurally plausible and visually coherent outputs.

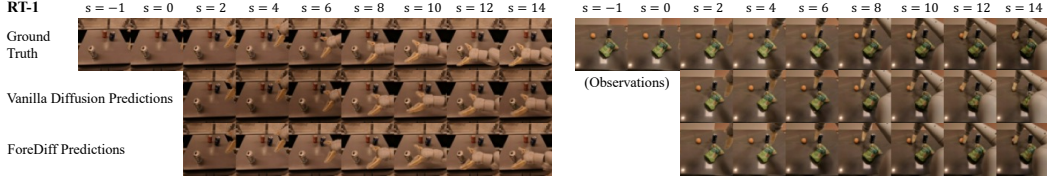


Figure 6: Visualization of results on RT-1 dataset (zoom in for details). Compared with vanilla diffusion, ForeDiff more accurately predicts the brightness of background and the position of robots.

STD_{SSIM} , and STD_{LPIPS} , defined as the standard deviation of metric values across multiple generated samples, to numerically represent sample consistency, where smaller values indicate more consistent predictions. See Appendix C for computation details.

Results. We present the experimental results in Table 1. ForeDiff outperforms vanilla diffusion in each dataset, showing not only an improvement in accuracy (PSNR, LPIPS, etc.) but a significant reduction in standard deviation (STD), which demonstrates its suitability for consistent world modeling. Moreover, there is no notable difference between ForeDiff-Zero and vanilla diffusion in terms of STD, suggesting that the improved consistency primarily stems from the deterministic pretraining procedure. The qualitative comparisons in Figures 5 and 6 further highlight the superior predictive ability of ForeDiff. Additionally, we compare ForeDiff with prior methods using their evaluation settings, where metrics are reported on the best of 100 samples (Top-1). As shown in Table 2, ForeDiff achieves competitive performance even without accounting for its advantages in consistency, further confirming its effectiveness as a general-purpose world model.

4.2 Scientific Spatiotemporal Forecasting

Setup. We then evaluate our method on HeterNS [21, 47] dataset, which is generated from simulations of heterogeneous 2D Navier-Stokes equations. Each sequence in HeterNS contains 20 frames with a resolution of 64×64 , where each pixel represents the vorticity of turbulence at the corresponding space. The task is to predict the latter 10 frames based on the first 10 frames. We report L2 and relative L2 as evaluation metrics according to previous works [21, 47].

Table 2: Addition results compared with baselines on RoboNet dataset. Metrics are reported on the best of 100 samples. LPIPS and SSIM scores are scaled by 100 for convenient display.

Method	FVD ↓	PSNR ↑	SSIM ↑	LPIPS ↓
MaskViT [14]	133.5	23.2	80.5	4.2
SVG [37]	123.2	23.9	87.8	6.0
GHVAE [41]	95.2	24.7	89.1	<u>3.6</u>
FitVid [5]	<u>62.5</u>	28.2	89.3	2.4
iVideoGPT [42]	<u>63.2</u>	<u>27.8</u>	90.6	4.9
ForeDiff	51.5	28.2	<u>90.4</u>	4.5

Table 3: Scientific spatiotemporal forecasting results on HeterNS dataset. Metrics are scaled by 100 for convenient display.

Method	L2 ↓	Relative L2 ↓
Vanilla Diffusion	1.73	1.50
ForeDiff-zero	1.03	0.83
ForeDiff	0.19	0.18

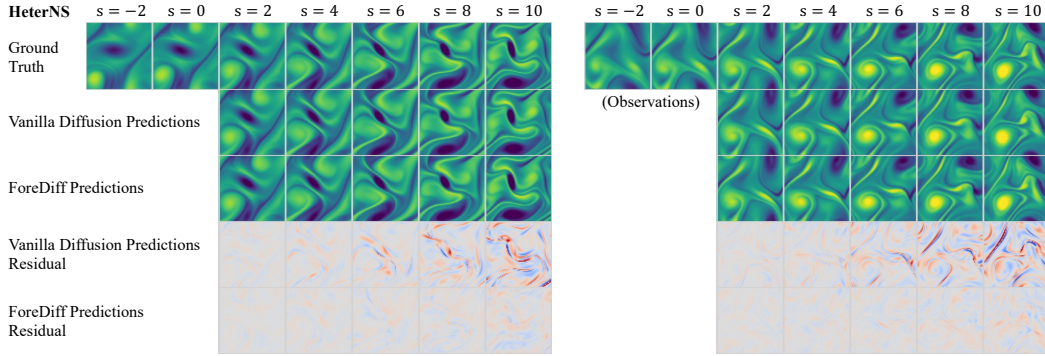


Figure 7: Visualization of results on HeterNS dataset (zoom in for details). As the simulation progresses, predictions from vanilla diffusion deviate increasingly from the ground truth, whereas ForeDiff maintains consistently accurate predictions.

Results. We present the experimental results in Table 3. ForeDiff achieves a much lower relative L2 error compared to ForeDiff-Zero, and both significantly outperform vanilla diffusion. These results suggest that incorporating deterministic blocks and pre-training them individually contribute to improved performance, demonstrating the applicability of ForeDiff for physical scenarios. Figure 7 illustrates the qualitative advantage of ForeDiff through visual comparisons.

4.3 Analysis

Effect of PredHead module. We investigate whether the predictive ability of the ViT stream, represented by its learned internal features, or its explicit prediction output contributes more to ForeDiff’s superiority. To this end, we conduct an ablation study on the PredHead module for training the DiT stream, which replaces internal representations with explicit prediction outputs as conditioning signals. As shown in Figure 8a, introducing the PredHead module leads to reduced model performance. This supports our hypothesis that the learned predictive representations, rather than the explicit prediction outputs, are more beneficial to the generative process.

Effect of ViT block number. To explore to what extent the predictive ability is required to benefit the generative process, we vary the number of ViT blocks M in the predictive stream from $M = 0$ (i.e., vanilla diffusion) to $M = 12$, while keeping the number of DiT blocks in the generative stream fixed. As shown in Figure 8b, adding a moderate number of ViT blocks noticeably improves performance, but further increasing M yields diminishing gains. This suggests that the predictive ability required to assist a fixed generative backbone can be achieved with minimal overhead, and that even a lightweight deterministic auxiliary module can provide meaningful improvements.

Effect of design beyond parameter scaling. We aim to validate that the performance gains of ForeDiff are attributable to its architectural design rather than the simple scaling of parameters. To isolate the effect of parameter scaling, we extend the vanilla diffusion model to 18 DiT blocks to match the total number of layers used in ForeDiff, and compare its performance with both ForeDiff-Zero and ForeDiff under identical ViT/DiT block configurations. We also evaluate the standalone

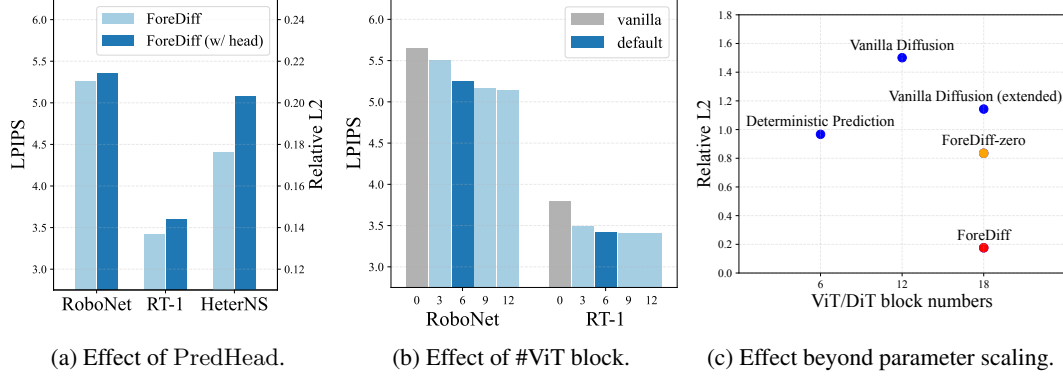


Figure 8: Ablation studies. (a) Adding PredHead leads to degraded performance. (b) Increasing #ViT block improves accuracy up to a point but additional blocks offer diminishing gains. (c) ForeDiff outperforms both an extended vanilla diffusion and the standalone deterministic predictor.

deterministic predictive stream used in ForeDiff. As shown in Figure 8c, ForeDiff outperforms both the extended vanilla diffusion model and the deterministic stream by a substantial margin. These results indicate that the combination of deterministic prediction and conditional diffusion contributes synergistically, highlighting the effectiveness of the proposed hybrid architecture for world modeling.

5 Related Work

Diffusion-based world models. Diffusion models have been widely adopted for world modeling tasks. Earlier approaches based on U-Net backbones investigated different strategies for incorporating conditioning signals, such as concatenation- and modulation-based fusion [38, 17, 6]. More recently, transformer-based diffusion models [27] have gained traction in world modeling [26, 44], offering improved scalability and support for multimodal inputs. These works mainly focus on architectural adaptation and employ relatively simple conditioning mechanisms. In contrast, our work addresses a more fundamental limitation of predictive ability within the diffusion modeling framework, without introducing additional design complexity beyond existing modules of DiT and ViT.

Non-diffusion world models. Beyond diffusion-based approaches, various frameworks have been proposed for world modeling, including RNN-based [31, 37, 39], auto-regressive [43, 42], and mask-based [14, 45] methods. As discussed in Section 3.1, diffusion models serve as strong baselines but tend to exhibit greater sample variability compared to these non-diffusion counterparts. This observation motivates our focus on enhancing consistency within diffusion-based world models.

Involvement of diffusion models as part. While many approaches adopt diffusion models in an end-to-end fashion, recent work has explored integrating them as auxiliary modules within broader architectures. For example, Li et al. [20] and Liu et al. [24] incorporate diffusion loss for image mask reconstruction and auto-regressive time-series forecasting, respectively, leveraging their generative strength in a modular fashion. In contrast, Foresight Diffusion treats the diffusion model as the central component and enhances its consistency by introducing auxiliary deterministic modules tailored for condition understanding in world modeling.

6 Conclusion

We proposed Foresight Diffusion (ForeDiff), a framework that improves consistency in diffusion-based world models by decoupling condition understanding from target denoising. Through a hybrid architecture that separates predictive and generative processes, and a two-stage training scheme that leverages pretrained deterministic predictors, ForeDiff overcomes key limitations of vanilla diffusion models—particularly their suboptimal predictive ability and high sample variance. Extensive experiments across real-world robot video prediction and scientific forecasting demonstrate that ForeDiff achieves superior accuracy and significantly enhanced sample-level consistency, marking a step toward more reliable and controllable diffusion-based world models.

References

- [1] Niket Agarwal, Arslan Ali, Maciej Bala, Yogesh Balaji, Erik Barker, Tiffany Cai, Prithvijit Chattopadhyay, Yongxin Chen, Yin Cui, Yifan Ding, et al. Cosmos world foundation model platform for physical ai. *arXiv*, 2025.
- [2] Sumukh K Aithal, Pratyush Maini, Zachary Lipton, and J Zico Kolter. Understanding hallucinations in diffusion models through mode interpolation. In *NeurIPS*, 2024.
- [3] Michael S Albergo and Eric Vanden-Eijnden. Building normalizing flows with stochastic interpolants. In *ICLR*, 2023.
- [4] Michael S Albergo, Nicholas M Boffi, and Eric Vanden-Eijnden. Stochastic interpolants: A unifying framework for flows and diffusions. *arXiv*, 2023.
- [5] Mohammad Babaeizadeh, Mohammad Taghi Saffar, Suraj Nair, Sergey Levine, Chelsea Finn, and Dumitru Erhan. Fitvid: Overfitting in pixel-level video prediction. *arXiv*, 2021.
- [6] Andreas Blattmann, Robin Rombach, Huan Ling, Tim Dockhorn, Seung Wook Kim, Sanja Fidler, and Karsten Kreis. Align your latents: High-resolution video synthesis with latent diffusion models. In *CVPR*, 2023.
- [7] Anthony Brohan, Noah Brown, Justice Carbajal, Yevgen Chebotar, Joseph Dabis, Chelsea Finn, Keerthana Gopalakrishnan, Karol Hausman, Alex Herzog, Jasmine Hsu, Julian Ibarz, Brian Ichter, Alex Irpan, Tomas Jackson, Sally Jesmonth, Nikhil Joshi, Ryan Julian, Dmitry Kalashnikov, Yuheng Kuang, Isabel Leal, Kuang-Huei Lee, Sergey Levine, Yao Lu, Utsav Malla, Deeksha Manjunath, Igor Mordatch, Ofir Nachum, Carolina Parada, Jodilyn Peralta, Emily Perez, Karl Pertsch, Jornell Quiambao, Kanishka Rao, Michael Ryoo, Grecia Salazar, Pannag Sanketi, Kevin Sayed, Jaspiar Singh, Sumedh Sontakke, Austin Stone, Clayton Tan, Huong Tran, Vincent Vanhoucke, Steve Vega, Quan Vuong, Fei Xia, Ted Xiao, Peng Xu, Sichun Xu, Tianhe Yu, and Brianna Zitkovich. Rt-1: Robotics transformer for real-world control at scale. *arXiv*, 2022.
- [8] Xinyuan Chen, Yaohui Wang, Lingjun Zhang, Shaobin Zhuang, Xin Ma, Jiashuo Yu, Yali Wang, Dahua Lin, Yu Qiao, and Ziwei Liu. Seine: Short-to-long video diffusion model for generative transition and prediction. In *ICLR*, 2023.
- [9] Sudeep Dasari, Frederik Ebert, Stephen Tian, Suraj Nair, Bernadette Bucher, Karl Schmeckpeper, Siddharth Singh, Sergey Levine, and Chelsea Finn. Robonet: Large-scale multi-robot learning. In *CoRL*, 2019.
- [10] Prafulla Dhariwal and Alexander Nichol. Diffusion models beat gans on image synthesis. In *NeurIPS*, 2021.
- [11] Alexey Dosovitskiy, Lucas Beyer, Alexander Kolesnikov, Dirk Weissenborn, Xiaohua Zhai, Thomas Unterthiner, Mostafa Dehghani, Matthias Minderer, Georg Heigold, Sylvain Gelly, et al. An image is worth 16x16 words: Transformers for image recognition at scale. In *ICLR*, 2020.
- [12] Frederik Ebert, Chelsea Finn, Sudeep Dasari, Annie Xie, Alex Lee, and Sergey Levine. Visual foresight: Model-based deep reinforcement learning for vision-based robotic control. *arXiv*, 2018.
- [13] Zhihan Gao, Xingjian Shi, Boran Han, Hao Wang, Xiaoyong Jin, Danielle Maddix, Yi Zhu, Mu Li, and Yuyang Bernie Wang. Prediff: Precipitation nowcasting with latent diffusion models. In *NeurIPS*, 2023.
- [14] Agrim Gupta, Stephen Tian, Yunzhi Zhang, Jiajun Wu, Roberto Martín-Martín, and Li Fei-Fei. Maskvit: Masked visual pre-training for video prediction. In *ICLR*, 2023.
- [15] Noriaki Hirose, Fei Xia, Roberto Martín-Martín, Amir Sadeghian, and Silvio Savarese. Deep visual mpc-policy learning for navigation. In *RA-L*, 2019.
- [16] Jonathan Ho, Ajay Jain, and Pieter Abbeel. Denoising diffusion probabilistic models. In *NeurIPS*, 2020.

- [17] Jonathan Ho, Tim Salimans, Alexey Gritsenko, William Chan, Mohammad Norouzi, and David J Fleet. Video diffusion models. In *NeurIPS*, 2022.
- [18] Quan Huynh-Thu and Mohammed Ghanbari. Scope of validity of psnr in image/video quality assessment. In *Electronics letters*, 2008.
- [19] Tero Karras, Miika Aittala, Timo Aila, and Samuli Laine. Elucidating the design space of diffusion-based generative models. In *NeurIPS*, 2022.
- [20] Tianhong Li, Yonglong Tian, He Li, Mingyang Deng, and Kaiming He. Autoregressive image generation without vector quantization. In *NeurIPS*, 2024.
- [21] Zongyi Li, Nikola Kovachki, Kamyar Azizzadenesheli, Burigede Liu, Kaushik Bhattacharya, Andrew Stuart, and Anima Anandkumar. Fourier neural operator for parametric partial differential equations. In *ICLR*, 2021.
- [22] Yaron Lipman, Ricky TQ Chen, Heli Ben-Hamu, Maximilian Nickel, and Matt Le. Flow matching for generative modeling. In *ICML*, 2023.
- [23] Xingchao Liu, Chengyue Gong, and Qiang Liu. Flow straight and fast: Learning to generate and transfer data with rectified flow. In *ICLR*, 2023.
- [24] Yong Liu, Guo Qin, Zhiyuan Shi, Zhi Chen, Caiyin Yang, Xiangdong Huang, Jianmin Wang, and Mingsheng Long. Sundial: A family of highly capable time series foundation models. In *ICLR*, 2025.
- [25] Nanye Ma, Mark Goldstein, Michael S Albergo, Nicholas M Boffi, Eric Vanden-Eijnden, and Saining Xie. Sit: Exploring flow and diffusion-based generative models with scalable interpolant transformers. In *ECCV*, 2024.
- [26] OpenAI. Sora: Video generation models as world simulators. <https://openai.com/research/video-generation-models-as-world-simulators>, 2024. Accessed: 2024-04-01.
- [27] William Peebles and Saining Xie. Scalable diffusion models with transformers. In *ICCV*, 2023.
- [28] Robin Rombach, Andreas Blattmann, Dominik Lorenz, Patrick Esser, and Björn Ommer. High-resolution image synthesis with latent diffusion models. In *CVPR*, 2022.
- [29] Robin Rombach, Andreas Blattmann, Dominik Lorenz, Patrick Esser, and Björn Ommer. High-resolution image synthesis with latent diffusion models. In *CVPR*, 2022.
- [30] Chitwan Saharia, William Chan, Saurabh Saxena, Lala Li, Jay Whang, Emily L Denton, Kamyar Ghasemipour, Raphael Gontijo Lopes, Burcu Karagol Ayan, Tim Salimans, et al. Photorealistic text-to-image diffusion models with deep language understanding. In *NeurIPS*, 2022.
- [31] Xingjian Shi, Zhourong Chen, Hao Wang, Dit-Yan Yeung, Wai-Kin Wong, and Wang-chun Woo. Convolutional lstm network: A machine learning approach for precipitation nowcasting. In *NeurIPS*, 2015.
- [32] Uriel Singer, Adam Polyak, Thomas Hayes, Xi Yin, Jie An, Songyang Zhang, Qiyuan Hu, Harry Yang, Oron Ashual, Oran Gafni, et al. Make-a-video: Text-to-video generation without text-video data. In *ICLR*, 2022.
- [33] Jascha Sohl-Dickstein, Eric Weiss, Niru Maheswaranathan, and Surya Ganguli. Deep unsupervised learning using nonequilibrium thermodynamics. In *ICML*, 2015.
- [34] Yang Song and Stefano Ermon. Generative modeling by estimating gradients of the data distribution. In *NeurIPS*, 2019.
- [35] Yang Song, Jascha Sohl-Dickstein, Diederik P Kingma, Abhishek Kumar, Stefano Ermon, and Ben Poole. Score-based generative modeling through stochastic differential equations. In *ICLR*, 2020.

- [36] Thomas Unterthiner, Sjoerd Van Steenkiste, Karol Kurach, Raphael Marinier, Marcin Michalski, and Sylvain Gelly. Towards accurate generative models of video: A new metric & challenges. *arXiv*, 2018.
- [37] Ruben Villegas, Arkanath Pathak, Harini Kannan, Dumitru Erhan, Quoc V Le, and Honglak Lee. High fidelity video prediction with large stochastic recurrent neural networks. In *NeurIPS*, 2019.
- [38] Vikram Voleti, Alexia Jolicoeur-Martineau, and Chris Pal. Mcvd-masked conditional video diffusion for prediction, generation, and interpolation. In *NeurIPS*, 2022.
- [39] Yunbo Wang, Haixu Wu, Jianjin Zhang, Zhifeng Gao, Jianmin Wang, S Yu Philip, and Mingsheng Long. Predrnn: A recurrent neural network for spatiotemporal predictive learning. In *TPAMI*, 2022.
- [40] Zhou Wang, Alan C Bovik, Hamid R Sheikh, and Eero P Simoncelli. Image quality assessment: from error visibility to structural similarity. In *TIP*, 2004.
- [41] Bohan Wu, Suraj Nair, Roberto Martin-Martin, Li Fei-Fei, and Chelsea Finn. Greedy hierarchical variational autoencoders for large-scale video prediction. In *CVPR*, 2021.
- [42] Jialong Wu, Shaofeng Yin, Ningya Feng, Xu He, Dong Li, Jianye Hao, and Mingsheng Long. ivideogpt: Interactive videogpts are scalable world models. In *NeurIPS*, 2024.
- [43] Wilson Yan, Yunzhi Zhang, Pieter Abbeel, and Aravind Srinivas. Videogpt: Video generation using vq-vae and transformers. In *CVPR*, 2021.
- [44] Zhuoyi Yang, Jiayan Teng, Wendi Zheng, Ming Ding, Shiyu Huang, Jiazheng Xu, Yuanming Yang, Wenyi Hong, Xiaohan Zhang, Guanyu Feng, et al. Cogvideox: Text-to-video diffusion models with an expert transformer. *arXiv*, 2024.
- [45] Lijun Yu, Yong Cheng, Kihyuk Sohn, José Lezama, Han Zhang, Huiwen Chang, Alexander G Hauptmann, Ming-Hsuan Yang, Yuan Hao, Irfan Essa, et al. Magvit: Masked generative video transformer. In *CVPR*, 2023.
- [46] Richard Zhang, Phillip Isola, Alexei A Efros, Eli Shechtman, and Oliver Wang. The unreasonable effectiveness of deep features as a perceptual metric. In *CVPR*, 2018.
- [47] Hang Zhou, Yuezhou Ma, Haixu Wu, Haowen Wang, and Mingsheng Long. Unisolver: Pde-conditional transformers are universal pde solvers. In *ICML*, 2025.

A Proof of Lemma

In this section we present the proof of Lemma 3.1.

Proof. The proof is structured in three parts: (1) $\hat{\mathbf{x}}$ reparameterization, (2) the ϵ -agnostic property of the optimal solution $\hat{\mathbf{x}}_\theta$, and (3) the reduction to a deterministic prediction model f_ξ in practice.

Starting from definition $\hat{\mathbf{x}}_\theta(\mathbf{x}_t, t, \mathbf{y}) = \mathbf{x}_t - t \cdot \mathbf{v}_\theta(\mathbf{x}_t, t, \mathbf{y})$ with $\mathbf{x}_t = (1 - t)\mathbf{x}_0 + t\epsilon$, it holds that

$$\begin{aligned}\mathcal{L}_{\text{pred}}(\theta) &= \mathbb{E}_{\mathbf{x}_0, \mathbf{y}, \epsilon, t} \left[\left\| \hat{\mathbf{v}}_\theta(\mathbf{x}_t, t, \mathbf{y}) - (-\mathbf{x}_0 + \epsilon) \right\|_2^2 \right] \\ &= \mathbb{E}_{\mathbf{x}_0, \mathbf{y}, \epsilon, t} \left[\left\| \frac{\hat{\mathbf{x}}_\theta(\mathbf{x}_t, t, \mathbf{y}) - \mathbf{x}_t}{t} - \frac{\mathbf{x}_0 - \mathbf{x}_t}{t} \right\|_2^2 \right] \\ &= \mathbb{E}_{\mathbf{x}_0, \mathbf{y}, \epsilon, t} \left[\frac{1}{t^2} \left\| \hat{\mathbf{x}}_\theta(\mathbf{x}_t, t, \mathbf{y}) - \mathbf{x}_0 \right\|_2^2 \right],\end{aligned}$$

and by letting $t = T$ we arrive

$$\mathcal{L}_{\text{pred}}(\theta|T) = \mathbb{E}_{\mathbf{x}_0, \mathbf{y}, \epsilon} \left[\left\| \hat{\mathbf{x}}_\theta(\mathbf{x}_1, 1, \mathbf{y}) - \mathbf{x}_0 \right\|_2^2 \right] = \mathbb{E}_{\mathbf{x}_0, \mathbf{y}, \epsilon} \left[\left\| \hat{\mathbf{x}}_\theta(\epsilon, 1, \mathbf{y}) - \mathbf{x}_0 \right\|_2^2 \right].$$

Since ϵ is independent to both network input \mathbf{y} and target \mathbf{x}_0 , the involvement of ϵ contributes no information in case of $t = T$, which matches the intuition that ϵ is sampled randomly.

Further notice the bias-variance decomposition

$$\begin{aligned}\mathbb{E}_{\mathbf{x}_0, \mathbf{y}, \epsilon} \left[\left\| \hat{\mathbf{x}}_\theta(\epsilon, 1, \mathbf{y}) - \mathbf{x}_0 \right\|_2^2 \right] &= \mathbb{E}_{\mathbf{y}} \left[\left\| \mathbb{E}_{\epsilon} [\hat{\mathbf{x}}_\theta(\epsilon, 1, \mathbf{y})] - \mathbb{E}_{\mathbf{x}_0|\mathbf{y}} [\mathbf{x}_0] \right\|_2^2 \right. \\ &\quad \left. + \mathbb{D}_{\epsilon} [\hat{\mathbf{x}}_\theta(\epsilon, 1, \mathbf{y})] + \mathbb{D}_{\mathbf{x}_0|\mathbf{y}} [\mathbf{x}_0] \right]\end{aligned}$$

By the convexity of the ℓ_2 loss, there exists $\bar{\epsilon}_0(\mathbf{y})$ satisfying

$$\left\| \hat{\mathbf{x}}_\theta(\bar{\epsilon}_0(\mathbf{y}), 1, \mathbf{y}) - \mathbb{E}_{\mathbf{x}_0|\mathbf{y}} [\mathbf{x}_0] \right\|_2^2 \leq \left\| \mathbb{E}_{\epsilon} [\hat{\mathbf{x}}_\theta(\epsilon, 1, \mathbf{y})] - \mathbb{E}_{\mathbf{x}_0|\mathbf{y}} [\mathbf{x}_0] \right\|_2^2.$$

Therefore,

$$\begin{aligned}\mathcal{L}_{\text{pred}}(\theta|T) &\geq \mathbb{E}_{\mathbf{y}} \left[\left\| \mathbb{E}_{\epsilon} [\hat{\mathbf{x}}_\theta(\epsilon, 1, \mathbf{y})] - \mathbb{E}_{\mathbf{x}_0|\mathbf{y}} [\mathbf{x}_0] \right\|_2^2 + \mathbb{D}_{\mathbf{x}_0|\mathbf{y}} [\mathbf{x}_0] \right] \\ &\geq \mathbb{E}_{\mathbf{y}} \left[\left\| \hat{\mathbf{x}}_\theta(\bar{\epsilon}_0(\mathbf{y}), 1, \mathbf{y}) - \mathbb{E}_{\mathbf{x}_0|\mathbf{y}} [\mathbf{x}_0] \right\|_2^2 + \mathbb{D}_{\mathbf{x}_0|\mathbf{y}} [\mathbf{x}_0] \right] \\ &= \mathbb{E}_{\mathbf{x}_0, \mathbf{y}} \left[\left\| \hat{\mathbf{x}}_\theta(\bar{\epsilon}_0(\mathbf{y}), 1, \mathbf{y}) - \mathbf{x}_0 \right\|_2^2 \right],\end{aligned}$$

i.e., the loss of diffusion models at $t = 1$ is bounded by that of a certain deterministic model $f(\mathbf{y}) = \hat{\mathbf{x}}_\theta(\bar{\epsilon}_0(\mathbf{y}), 1, \mathbf{y})$ which minimizes the following objective:

$$\mathcal{L}_{\text{deter}} = \mathbb{E}_{\mathbf{x}_0, \mathbf{y}} \left[\left\| f(\mathbf{y}) - \mathbf{x}_0 \right\|_2^2 \right].$$

Finally we prove that the inequalities can become an equalities in practical network architectures, which requires $\hat{\mathbf{x}}_\theta(\epsilon_1, 1, \mathbf{y}) = \hat{\mathbf{x}}_\theta(\epsilon_2, 1, \mathbf{y})$ for any ϵ_1, ϵ_2 . Considering the first layer to process ϵ as $W\epsilon + b$, it is sufficient to set the weight W to zero values, and further by setting b and 1 as new network parameters, $\hat{\mathbf{x}}_\theta(\epsilon_1, 1, \mathbf{y})$ can be reduced into a deterministic model f_ξ , completing the proof. \square

Table 4: Architecture and training details of the pretrained autoencoder for each dataset.

	RoboNet	RT-1	HeterNS
Parameters		55M	
Resolution		64×64	
Input channels	3	3	1
Latent channels		3	
Down blocks		3	
Down layers per block		2	
Down channels		[128, 256, 512]	
Mid block attention		True	
Up blocks		3	
Up layers per block		2	
Up channels		[512, 256, 128]	
Normalization		GroupNorm	
Norm groups		32	
Activation		SiLU	
Training steps	5×10^6	3×10^6	3×10^6
Discriminator start step		5×10^4	
Batch size		16	
Learning rate		4×10^{-5}	
LR schedule		Constant	
Optimizer		AdamW	

B Implementation Details

We adopt the widely used latent diffusion paradigm, which operates in a compressed latent space and relies on a pretrained autoencoder consisting of an encoder and a decoder. The autoencoder downsamples the input by a factor of 4×4 and maps it to a latent representation with 3 channels. All prediction and denoising operations are performed in this latent space. The autoencoder architecture follows the standard design of Stable Diffusion [29], and dataset-specific architectural and training details are summarized in Table 4.

Our main model follows the DiT [27] and ViT [11] architecture families, using a unified design across all tasks. We adopt ViT-S and DiT-S configurations for the predictive and generative streams, respectively. Patch embeddings are extracted using a minimal PatchEmbed module that partitions inputs into non-overlapping 2×2 patches, followed by a linear projection. Sinusoidal positional encodings are used, with embedding dimensions partitioned in a 3:3:2 ratio among the two spatial axes and the temporal axis. Detailed block settings are shown in Table 5. All models are trained using the AdamW optimizer with a constant learning rate of 1×10^{-4} and dataset-specific training steps (see Appendix C).

Table 5: Architecture settings for ViT-S and DiT-S blocks used in ForeDiff.

	ViT-S (predictive stream)	DiT-S (generative stream)
Number of blocks	6	12
Hidden size	384	384
MLP ratio	4.0	4.0
Attention heads	6	6
Positional encoding	Sinusoidal	Sinusoidal
Normalization	LayerNorm	AdaLN
Activation	SiLU	SiLU

To construct the conditioning input, we follow the masking-based strategy introduced in prior work [6]. Specifically, a temporal binary mask $\mathbf{m} \in \{0, 1\}^{O+S}$ is defined over the full sequence $\mathbf{s}^{-O+1:S}$ to indicate which frames are observed (condition) and which are to be predicted (target), where O and S denote the numbers of observed and future frames, respectively. After encoding the full sequence into

the latent space via $\mathbf{z} = E(\mathbf{s}^{-O+1:S}) \in \mathbb{R}^{(O+S) \times C \times H \times W}$, we apply the mask \mathbf{m} along the temporal axis by computing $\mathbf{z}_{\text{cond}} = \mathbf{m} \cdot \mathbf{z}$, where the mask is broadcast across spatial and channel dimensions. To make the temporal structure explicit, we further concatenate the binary mask itself (channel-wise) to the masked latent \mathbf{z}_{cond} , and feed the result into the predictive stream.

When additional conditioning inputs such as actions or goals \mathbf{c} are available (e.g., in RoboNet and RT-1), we directly concatenate them with the masked latent \mathbf{z}_{cond} along the channel axis. This enables the model to jointly reason over visual history and auxiliary task-specific signals.

Overall, this masking-based design supports a unified conditioning mechanism for both video-only and video+action tasks. The masked latent input, along with any auxiliary information (e.g., actions), is processed by the predictive stream to produce intermediate features \mathbf{g}_M , which serve as conditioning signals for the generative stream.

To inject this condition information into the generative stream, we use a lightweight Fusion module composed of an adaptive layer normalization (AdaLN) layer followed by a two-layer MLP with GELU activation. The fusion operation is defined as:

$$\mathbf{h}_1 = \text{MLP}(\text{AdaLN}([\mathbf{h}_0; \mathbf{g}_M], t)), \quad (9)$$

where \mathbf{h}_0 denotes the noisy target, \mathbf{g}_M is the output of the predictive stream (prior to the PredHead module), and t is the diffusion timestep. We first concatenate \mathbf{h}_0 and \mathbf{g}_M , apply AdaLN conditioned on t , and then pass the normalized features through the MLP to obtain the fused representation.

C Experimental Setup

We evaluate ForeDiff on three benchmark datasets covering both real-world and simulated spatiotemporal dynamics: RoboNet [9], RT-1 [7], and HeterNS [21, 47]. This section provides additional details on dataset setups, task configurations, and evaluation metrics. All experiments are conducted in a single NVIDIA-A100 40G GPU.

RoboNet. RoboNet is a large-scale real-world video dataset for vision-based robotic manipulation, consisting of approximately 162,000 trajectories collected across seven different robot platforms from four institutions. Each trajectory includes RGB video frames and associated action sequences, all represented in a unified end-effector control space. The dataset captures a wide range of variations in robot embodiment (e.g., Sawyer, Kuka, Franka), gripper design, camera viewpoints, surfaces, and lighting conditions.

Following prior works [5, 42], we resize all frames to 64×64 and predict 10 future frames based on 2 observed frames and corresponding actions. All models are trained on RoboNet for 1×10^6 steps with a batch size of 16. We report PSNR, SSIM, LPIPS, and FVD as evaluation metrics. In addition, we compute standard deviation (STD) across multiple samples to quantify sample consistency.

RT-1. RT-1 is a large-scale real-world robotics dataset comprising over 130,000 episodes collected from a fleet of 13 mobile manipulators performing diverse manipulation tasks in office kitchen environments. Each episode includes an RGB video sequence, a natural language instruction, and the executed robot actions. The dataset covers over 700 distinct tasks involving object interaction, long-horizon manipulation, and routine execution.

We formulate the prediction task by conditioning on 2 observed frames and a task instruction, and predicting the next 14 frames. All frames are resized to 64×64 . Training on RT-1 is conducted for 5×10^5 steps with a batch size of 16, and the evaluation protocol matches that of RoboNet, using PSNR, SSIM, LPIPS, FVD, and STD of these metrics across samples.

HeterNS. HeterNS is a synthetic dataset generated by numerically solving the two-dimensional incompressible Navier–Stokes equations in vorticity formulation over a periodic domain. The governing system is defined as:

$$\partial_t w(x, t) + u(x, t) \cdot \nabla w(x, t) = \nu \Delta w(x, t) + f(x), \quad x \in (0, 1)^2, \quad t \in (0, T], \quad (10a)$$

$$\nabla \cdot u(x, t) = 0, \quad x \in (0, 1)^2, \quad t \in [0, T], \quad (10b)$$

$$w(x, 0) = w_0(x), \quad x \in (0, 1)^2, \quad (10c)$$

where w is the vorticity field, u is the divergence-free velocity field recovered via the stream function ψ satisfying $\Delta\psi = -w$, ν is the viscosity coefficient, and $f(x)$ is a time-invariant external forcing term.

To construct a diverse collection of PDE instances, we vary two key physical parameters: the viscosity ν and the structure of the forcing term $f(x)$. Specifically, the training set is constructed from a Cartesian grid of parameter configurations:

$$\nu \in \{1 \times 10^{-5}, 1 \times 10^{-4}, 1 \times 10^{-3}\}, \quad f(x) \in \{5 \text{ distinct variants}\},$$

yielding a total of $3 \times 5 = 15$ unique PDE settings.

Among the forcing terms, three are defined as:

$$f(x) = 0.1 (\sin(\omega_1 \pi(x_1 + x_2)) + \cos(\omega_2 \pi(x_1 + x_2))),$$

with frequency pairs $(\omega_1, \omega_2) \in \{(2, 2), (2, 4), (4, 4)\}$. The fourth variant is defined as:

$$f(x) = 0.1 (\sin(2\pi(x_1 - x_2)) + \cos(2\pi(x_1 - x_2))),$$

and the fifth as:

$$f(x) = 0.1 (\sin(2\pi(x_1^2 + x_2^2)) - \cos(2\pi(x_1^2 + x_2^2))).$$

These five variants cover a range of spatial patterns, including directional, cross-diagonal, and radially symmetric forcings.

For each of the 15 configurations, we simulate 1000 trajectories, resulting in a total of 15,000 samples. Each trajectory consists of 20 vorticity fields at a spatial resolution of 64×64 . The prediction task involves forecasting the final 10 frames given the first 10 as context. Each model is trained for 5×10^5 steps using a batch size of 16.

Evaluation metrics. We adopt a suite of evaluation metrics to assess model performance across multiple dimensions, including visual quality, perceptual fidelity, predictive accuracy, and sample consistency. These include PSNR, SSIM, LPIPS, FVD, Relative L2, and STD, described as follows:

- **Peak Signal-to-Noise Ratio (PSNR)** [18] quantifies the ratio between the maximum possible pixel intensity and the distortion introduced by reconstruction errors. It is defined in logarithmic scale (dB) and commonly used to evaluate frame-wise reconstruction quality. A higher PSNR value indicates less pixel-level distortion and better fidelity to the original ground truth frame.
- **Structural Similarity Index Measure (SSIM)** [40] measures perceptual similarity by comparing luminance, contrast, and structural information between images. Unlike PSNR, SSIM better correlates with human visual perception. The SSIM score ranges from -1 to 1, where 1 denotes perfect structural similarity. For better readability, we scale SSIM scores by a factor of 100 in all reported results.
- **Learned Perceptual Image Patch Similarity (LPIPS)** [46] evaluates perceptual similarity using deep features extracted from a pretrained neural network (e.g., VGG or AlexNet). It computes the L2 distance between feature representations of two images, capturing differences beyond pixel values. Lower LPIPS values indicate better perceptual quality. Similar to SSIM, LPIPS scores are multiplied by 100 for display.
- **Fréchet Video Distance (FVD)** [36] extends the Fréchet Inception Distance (FID) to video generation by considering temporal dynamics. It compares the distributions of real and generated videos in a feature space extracted from a pretrained video recognition model. FVD is sensitive to both spatial quality and temporal consistency, making it a strong indicator of overall generative performance.
- **Relative L2 Distance** [21] captures normalized regression error in pixel or field-level prediction tasks. It is computed as:

$$\text{Relative L2} = \frac{\|\hat{x} - x\|_2}{\|x\|_2},$$

where \hat{x} and x denote the prediction and ground truth, respectively. A lower relative L2 value implies that the model produces more accurate outputs with respect to both magnitude and structure. This metric is particularly suited for scientific forecasting tasks such as fluid dynamics.

- **Standard Deviation (STD)** of metrics is used to evaluate sample consistency across multiple generations from the same condition. For each condition input (e.g., past frames and action/instruction), we generate N samples (typically $N = 100$), compute a chosen metric \mathcal{M} (e.g., PSNR, SSIM, LPIPS) for each sample, and calculate the standard deviation of these scores. Let $\mathcal{M}_1^{(i)}, \dots, \mathcal{M}_N^{(i)}$ denote the metric values for the i -th condition, the per-condition standard deviation is:

$$\text{STD}^{(i)} = \sqrt{\frac{1}{N} \sum_{j=1}^N \left(\mathcal{M}_j^{(i)} - \bar{\mathcal{M}}^{(i)} \right)^2}, \quad \text{where } \bar{\mathcal{M}}^{(i)} = \frac{1}{N} \sum_{j=1}^N \mathcal{M}_j^{(i)}.$$

The final STD score is then averaged over all C conditions:

$$\text{STD} = \frac{1}{C} \sum_{i=1}^C \text{STD}^{(i)}.$$

Lower STD indicates that the model produces more consistent outputs across stochastic samples, reflecting stronger reliability under the same input condition.

D More Experimental Results

This section provides the full numerical results corresponding to the analyses discussed in Section 4.3. While the main paper focuses on reporting key trends and visualizations, the tables below include complete metric values across datasets and variants, serving as a quantitative supplement.

Effect of PredHead module. Table 6 reports the full numerical results for the PredHead ablation across all datasets.

Table 6: Ablation results on the PredHead module. Across datasets, removing PredHead consistently improves both perceptual and pixel-wise metrics. SSIM, LPIPS, L2, and Relative L2 are scaled by 100.

Dataset	Method	FVD ↓	PSNR ↑	SSIM ↑	LPIPS ↓
RoboNet	ForeDiff	51.5	27.4	88.8	5.25
	ForeDiff (with PredHead)	53.7	27.3	88.7	5.35
RT-1	ForeDiff	12.0	31.2	94.4	3.42
	ForeDiff (with PredHead)	12.4	31.0	94.1	3.60
Dataset	Method	L2 ↓	Relative L2 ↓		
HeterNS	ForeDiff	0.19	0.18		
	ForeDiff (with PredHead)	0.23	0.20		

Effect of ViT block number. Table 7 presents detailed results of varying the number of predictive (ViT) blocks, while keeping the number of generative (DiT) blocks fixed.

Effect of design beyond parameter scaling. Table 8 provides the complete quantitative results for the ablation study on HeterNS dataset, used to isolate the effect of architectural design from mere parameter scaling.

E Limitations

While Foresight Diffusion demonstrates consistent improvements in both predictive accuracy and sample consistency, several aspects remain open for future exploration:

Use of pretrained predictors in latent space. In this work, the deterministic predictive stream is trained from scratch. This design choice is primarily due to the lack of pretrained models that operate directly in the latent space of our autoencoder, as well as the absence of task-aligned autoencoders for datasets such as RoboNet and HeterNS. Exploring the use of pretrained predictors—if appropriately adapted—could offer gains in training efficiency and generalization.

Table 7: Effect of varying ViT block number (denoted by M) on performance, with DiT blocks fixed to 12. Adding a moderate number of predictive blocks improves performance, while further increases yield diminishing returns. SSIM and LPIPS are scaled by 100.

Dataset	Method	FVD ↓	PSNR ↑	SSIM ↑	LPIPS ↓
RoboNet	M=0 (vanilla)	53.8	27.1	88.2	5.65
	M=3	53.3	27.1	88.3	5.51
	M=6 (default)	51.5	27.4	88.8	5.25
	M=9	50.8	27.5	89.0	5.17
	M=12	52.1	27.5	89.1	5.14
RT-1	M=0 (vanilla)	11.7	30.4	93.6	3.79
	M=3	11.8	31.0	94.2	3.49
	M=6 (default)	12.0	31.2	94.4	3.42
	M=9	12.4	31.3	94.4	3.41
	M=12	12.4	31.3	94.4	3.41

Table 8: Ablation results on HeterNS dataset. ForeDiff clearly outperforms both deterministic-only and extended vanilla diffusion models, confirming that its improvements stem from architectural design rather than model size alone. Metrics are scaled by 100.

Dataset	Method	L2 ↓	Relative L2 ↓
HeterNS	Vanilla Diffusion	1.73	1.50
	Deterministic Prediction	1.06	0.97
	ForeDiff-Zero	1.03	0.83
	ForeDiff	0.19	0.18
	Vanilla Diffusion (extended)	1.29	1.14

Evaluation limited to open-loop settings. Our experiments are conducted in open-loop prediction settings, where consistency is evaluated under fixed input conditions. While this setup is sufficient for assessing sample quality and robustness, we leave the investigation of ForeDiff in interactive or closed-loop scenarios (e.g., planning or decision-making) to future work, where stability under auto-regressive rollout may become even more important.

Scope limited to diffusion models. While our study focuses on diffusion-based world models, many of the key insights—especially regarding the entanglement of condition understanding and generative modeling—may generalize to other model families, such as auto-regressive or energy-based models. Extending similar architectural decoupling and predictive pretraining strategies to these settings may yield further improvements and warrants future investigation.